Efficient Field Emission from Vertically Aligned $Cu_2O_{1-\delta}$(111) Nanostructure Influenced by Oxygen Vacancy

Suman Nandy, Ranjit Thapa, Mohit Kumar, Tapobrata Som, Nenad Bundaleski, Orlando M. N. D. Teodoro, Rodrigo Martins, and Elvira Fortunato**

In the architecture described, cuprous oxide (Cu_2O) is tamed to be highly (111) plane oriented nanostructure through adjusting the deposition postulate by glancing angle deposition technique. In the controlled atmosphere oxygen vacancy is introduced into the Cu_2O crystal subsequently fostering an impurity energy state (E_{im}) close to the conduction band. Our model of Cu_2O electronic structure using density functional theory suggests that oxygen vacancies enhance the electron donating ability because of unshared *d*-electrons of Cu atoms (nearest to the vacancy site), allowing to pin the work function energy level around 0.28 eV compared to the bulk. This result is also complemented by Kelvin probe force microscopy analysis and X-ray photoelectron spectroscopy method. Oxygen vacancy in Cu_2O ($Cu_2O_{1-\delta}$) exhibits promising field emission properties with interesting field electron tunneling behavior at different applied fields. The films show very low turn-on and threshold voltages of value 0.8 and 2.4 V μm^{-1} respectively which is influenced by the oxygen vacancy. Here, a correlation between the work function modulation due to the oxygen vacancy and enhancement of field emission of $Cu_2O_{1-\delta}$ nanostructure is demonstrated. This work reveals a promising new vision for Cu_2O as a low power field emitter device.

1. Introduction

The growing role of nano-perspective in contemporary technologies is based on the smallest unit of matter to process new materials and device atom by atom in order to obtain exceptional performance influenced by the nanoscale architecture. Thus material dimensionality with well-defined structure and precisely controlled growth mechanism plays a critical role in nanotechnology due to its structure-dependent physical properties, for example, the different ways of electron transport mechanism in 3D, 2D, and 1D structures.[1–3] Owing to the fact that physical and geometrical parameters are highly responsible for the electron tunneling properties, nanomaterials with higher degree of engineering within nanoscale architecture may have potential application in field emission based devices such as flat panel display, microwave power amplifiers, electron microscopes as well as gas and mass sensors.[4–10] Till date, field emission from nanomaterial has been a subject of immense study for researchers based on the ground of high-tech display applications as well as on the deep theoretical interest to understand the electron mechanism of material. Since last two decades, field emission properties based on wide band gap and narrow band gap materials with different nanostructures have attracted prime interest of several research groups.[11,12] However, the field electron tunneling behavior for semiconductor emitter is more complicated due to effects from both of its minor and major carrier concentration, formation of impurity energy level and way of field penetration.

Field electron emission is a unique quantum mechanical effect, where electrons tunnel through a potential energy barrier at the solid-vacuum interface into the vacuum under an external electric field.[13] The efficiency of this emission process is tens of millions of times higher than in other known emission processes. This phenomenon occurs in high electric fields in the range of 10^7–10^8 V cm^{-1}. In order to produce such high fields using reasonable potentials, the emitter is usually formed into a tip with the apex radius of curvature ranging from tens of angstroms to several micrometers. The high electric field sufficiently narrows the potential barrier (which can be described as the zero electric field work function energy ϕ) at the metal–vacuum interface for the electrons to have a significant probability of tunneling from the solid into the vacuum, enabling the Fowler–Nordheim (F–N) tunneling.[13,14] Field emission from semiconductors is much more complicated process due to its low carrier concentration in bulk emitter compare with

Dr. S. Nandy, Prof. R. Martins, Prof. E. Fortunato
CENIMAT/I3N, Departmento de Ciência dos Materiais
Faculdade de Ciências e Tecnologia
FCT, Universidade Nova de Lisboa and
CEMOP-UNINOVA
2829–516, Caparica, Portugal
E-mail: snandy_ju@yahoo.co.in; emf@fct.unl.pt
Dr. R. Thapa
SRM Research Institute
SRM University
Kattankulathur, 603 203, Chennai, Tamil Nadu, India
M. Kumar, Prof. T. Som
Institute of Physics
Sachivalaya Marg, Bhubaneswar, Odisha 751-005, India
Dr. N. Bundaleski, Prof. O. M. N. D. Teodoro
CeFiTec, Departamento de Física
Faculdade de Ciências e Tecnologia
Universidade Nova de Lisboa
P-2829-516, Campus de Caparica, Caparica, Portugal

DOI: 10.1002/adfm.201402910

metal emitter. In the presence of external field, low carrier concentrations allow for field penetrating into the semiconductor, causing band bending and nonlinearity of current–voltage characteristics in F–N coordinates. The intercept of F–N plot, ln (J/E^2) versus $1/E$, contains electron emission related information about effective emission area and field enhancement factor. Here we report that strong and sustained cold electron emission at low applied electric filed is obtained from the cuprous oxide nanostructure thin film. Such low-field electron emission is achieved at a current density that is of interest to low-power flat panel display (LP-FPD) and other field emitter electronics.

In this study, we have evolved the field electron tunneling analyses of cuprous oxide (Cu_2O) nanostructure. Cu_2O has long been studied in both experimental and theoretical fields because of its attracting electronic configuration. Vacancies in stoichiometric Cu_2O systems are significant due to its impact on band structure hence influencing the electronic properties. Several theoretical groups[15–17] have shown their interest in this particular regime. Here, we attribute the electron emission behavior of Cu_2O thin film as an averaging effect of oxygen vacancy and highly oriented (111) nanostructure with tiny crumple surface. Formation of oxygen vacancy plays a lead role to the Fermi-level pinning[18–20] energy along with the formation of impurity energy states within the bulk band gap, causing an enhancement of electron emission at low field. A theoretical model has been developed to support our idea. Local deviation from electrical neutrality and weeny variation in surface potential of the thin film emitter surface create an enhancement of the localized electric field near the surface thereby reducing the threshold field. The local surface potential mapping has been shown by Kelvin probe force microscope (KPFM) with simultaneously measuring the surface topography.

2. Results and Discussions

2.1. Field Emission Performance

Most of the field emission studies from nanostructure semiconductors with low turn-on field (≈1.0 V μm^{-1}) are based on geometrical parameters[4,21–26] of the emitter which plays the most important role in field enhancement factor ($\beta = h/r$, where h is the height and r is the radius of the structure). However, field emission at lower electric field can also be influenced by Fermi level pinning and formation of localized electron trap level due to the defects mechanism. In this study, we have fabricated directional crumple-like cuprous oxide nanostructure using glancing angle deposition technique (GLAD).[1] We have performed the field emission measurements for several nanostructures with different deposition conditions to optimize the field electron emission enhancement factor. But, here we are only interested to analyze the best results for as grown optimized single phase Cu_2O (111) nanostructure. **Figure 1**a shows the cross-sectional FESEM view of typical Cu_2O nanostructure. Magnified images (inset) of the corresponding material shows that the structures were grown vertically with conical shape, having tiny crumple throughout the surface. This nanostructure is highly dependent on the working gas pressure (discussed in Supporting Information). But here we are only interested to enucleate the correlation of the electron tunneling behavior of Cu_2O nanostructure with oxygen vacancy. Recently, the group of Carter[27] and Wu et al.[28] have shown their theoretical interest on O vacancy in Cu_2O system. In this study, we are going to explain the field emission results with structural anomalies of the nanostructure material using our theoretical model.

In cold cathode emission process, electrons emitted from the cathode surface strike anode due to the applied electric field, which can modulate the potential barrier height at emitter surface–vacuum interface. Based on the F–N model, emission current from the semiconductor is attributed to the quantum tunneling effect of electrons from emitter surface into vacuum under the influence of external electric field. Schematic diagram of the system is shown in Figure 1b.

The FN equation can be expressed as[13]

$$J = \frac{AE_f^2}{\phi}\exp\left(-\frac{B\phi^{3/2}}{E_f}\right) \quad (1)$$

Here, J is the emission current density, $A = 1.54 \times 10^{-6}$ cm^2 A (mV^{-1})^2 eV and $B = 6.83 \times 10^9$ (V m^{-1}) eV$^{-3/2}$ are constants. The electric field E_f appearing in F–N expression can be described as the effective electric field, which is playing on the localized apex area of emitter surface

$$E_f = \beta E,\ E = \frac{V}{d} \quad (2)$$

where d is the anode to emitter spacing and V is the applied voltage between them. E is the corresponding external field. It has been generally assumed that the field enhancement factor β depends only on the emitter geometry and can play an important role to enhance the effective electric field on the apex area, causing high emission current. It can be also claimed that the work function (ϕ) of emitter surface at nanoscale regime influences the properties of field emission.

Information about electrons emission from the emitter-vacuum interface toward the metallic anode under an external applied voltage was achieved by the *J-E* (current density-applied field) characteristics. Figure 1c shows the field emission current density (J) versus applied field (E) at room temperature for typical three samples namely $Cu_2O_{1-\delta^1}$, $Cu_2O_{1-\delta^2}$, and $Cu_2O_{1-\delta^3}$ according to oxygen vacancy ($\delta^1 > \delta^2 > \delta^3$). A close look of *J–E* at lower field is shown in Figure 1d, indicating turn-on field (E_{to}) for each oxygen vacancy. The distance between emitter and anode was kept at 200 μm for all the samples. The *J–E* characteristics were determined for averaging of several data acquisitions to confirm the stability of emitter surface. The result shows a stable field current emission without effect of any residual surface electrons. The stability of field emission is of practical interest in sense of display device since the emitter surface can easily be damaged by localized thermal energy due to electron collision. A stable emission current for a typical sample at 1 mA cm^{-2} for 2 h has been shown in Figure S1, Supporting Information. Our reported value of turn-on field, E_{to} (field at which emission electrons from emitter can produce 10 μA cm^{-2} current density)[29] and threshold field, E_{th} (the field which is able to produce a current density of 1 mA cm^{-2}) are

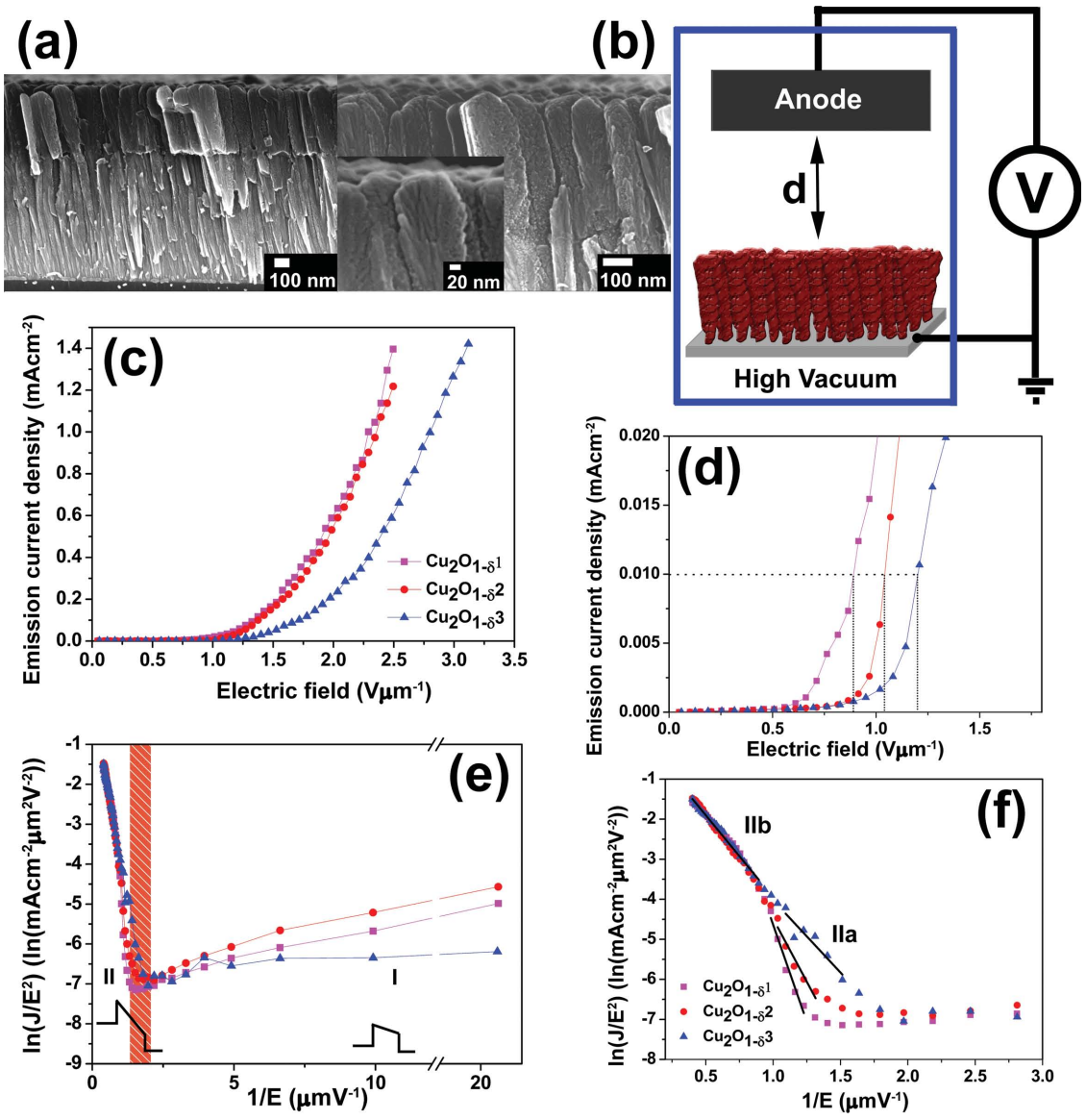

Figure 1. a) Cross-sectional FESEM image of the Cu_2O nanostructure with crumple surface (can be seen in inset). b) Schematic of the field emission measurement. c) Field emission current from Cu_2O nanostructure with oxygen vacancy (sample was denoted as $Cu_2O_1.\delta_n$, n = 1,2,3 according to the gradual decrease of vacancy concentration). d) The close look of turn-on field (E_{to}), where it is decreasing with increase of oxygen vacancy. e) F–N plot for electron tunneling from lower to higher field. Red dashed lines show the transition field above which the emission electrons obey the F–N tunneling mechanism. Schematic represents the shape of barrier at low and high bias fields. f) Represents further close inspection of electron tunneling nature at higher field which belongs to the semiconductor properties.

much lower, 0.8 and 2.4 V μm^{-1} respectively, when compared to others reports.[11,12,30,31] A recent survey on performance of Cu_2O base field emitter has been shown in **Table 1**.[4,30–32] A variation in field electron tunneling behavior has been observed with oxygen vacancy. Results show a decrement of turn-on field with increasing O vacancy. Gradual discussion will reveal that the work function (ϕ) has been pinned due to the creation of O vacancy in Cu_2O system, thereby enhancing the electron emission occurrence at ultralow field.

Figure 1e shows the corresponding F–N plot. Interestingly F–N plot of the field emission current from Cu_2O nanostructure displays two characteristics region with two different slopes. It therefore interprets that the emission process is not simply a F–N tunneling at the emitter surface, but also other contributing factors are involved.[33] Field emission from semiconductor is considerably more complicated as the emission current can be strongly influenced by state of the surface, field penetration into the semiconductor, limited availability of electrons, and by the fact that emission can arise from both conduction and valance bands. In particular, it can be suggested that as a p-type semiconductor there is much lower concentration of electrons in conduction band and most of the emission current caused due to trap-assisted electron transport energy level formation between the band gap. At low electric field (region I), electrons

Table 1. Turn-on (E_{to}) and Threshold (E_{th}) fields of Cu_2O based field emitter reported recently.

Emitter	E_{to} [V μm^{-1}] [μA cm^2]	E_{th} [V μm^{-1}] [mA cm^2]	Ref.
Cu_2O	9.6 at 10	11.7 at 1	Tang et al.[31]
Cu_2O micro/ nanocrystalline	3.1–3.5 at 0.1	11–12.1 at 1	Shi et al.[4]
Cu_2O niddle	8.4 at 10	11.8 at 0.1	Deo et al.[32]
Cu_2O–ZnO nanobrush	6.5 at 10	8.9 at 0.01	Deo et al.[32]
Cu_2O pure block	6.18–6.94 at 10	11.7–12 at 1	Wang et al.[30]
Cu_2O–ZnO nanoheterojunction	3.42 at 10	7.25 at 1	Wang et al.[30]

tunnel through the trapezoidal barrier indicating direct tunneling.[34,35] A striking change in tunneling behavior is observed after exceeding certain field (can be described by V_{trans}) showing linear behavior with comparatively higher slopes. Tunneling in the high-field region is synonymous with tunneling through a triangular barrier obeying the F–N tunneling.[35,36] This part is more complicated in terms of quantum mechanical tunneling for the present system. A detailed inspection on this part beyond V_{trans} shows two different slopes in Figure 1f. Region IIa with comparative lower slopes indicates that the emission current is determined by F–N tunneling at the surface due to the presence of enough electrons into the conduction band. Initially increasing field penetration in the semiconductor creates a depletion region, causing current limitation by the supply of electrons and not the transparency of barrier.[37,38] Moreover, for higher field in region IIb, a sharp rise in emission current has been appeared. The phenomenon can be considered for sufficient strong field which impacts on the ionization in space charge region, causing the rapid electron emission from the surface. At higher fields, free electron concentration near to the surface states rises considerably and can be supplied from the valance band. For semiconductor field emitter, field penetration can lead to a change of the carrier concentration in the near surface region and bending of the energy band at emitter-vacuum interface thus being a key factor to emission current.

2.2. Field Intensification

The nature of electron tunneling in ultralow field can be described by the nanostructure geometry formed by material and the defect mechanism due to vacancy formation in the structure. **Figure 2**a shows the topographical image of a typical emitter surface clearing a tiny series of grains, projecting as an apex layer, each acting as an individual emitter tip (3D image of the corresponding sample has been shown in Figure S2a, Supporting Information). The fields therefore will be distributed throughout the surface and generate a localized field intensification using Gaussian form of the electric field (schematic shown in Figure S2b, Supporting Information). Field intensification factor β depends on the geometry of emitters and the work function of emitter surface, which is independent of the applied field. The field enhancement factor β is calculated from the slope of low- and high-field region using Equation (1) and therefore be

$$\beta = \frac{B\phi^{3/2}}{\text{slope (F–N plot)}} \tag{3}$$

Assuming that the work function of $Cu_2O_{1-\delta}$ nanostructure is 4.97 eV (obeying the proposed theoretical model), the field enhancement factor is found to be 8600. Also the crumple surface of the emitter will behave like a tiny protrusion of the emitter, hence acting as an electron source. Each and every tiny nanostructure protrusion thus indulges in the field emission enhancement factor. However, electron tunneling is not fully dependent on nanostructure geometry when localized work function of the emitter is not the same. We have analyzed the local surface work function of the Cu_2O nanostructure thin film by Kelvin probe force microscopy (KPFM), a non-destructive scanning probe based technique that allows to minimize the electrostatic interaction between tip–surface at each scanning point on the sample surface by applying external DC voltage.[39,40] This yields the contact potential difference (CPD) between tip and surface, where U_{DC} = CPD = $(\phi_{sample} - \phi_{probe})/e$. Such a technique can directly interpret the localized work function of the surface at nano-scale region with simultaneous illustration of the sample topography. Here we have focused on the qualitative analysis of the surface potential mapping of typical Cu_2O thin film with [Cu]/[O] > 2.0 (Figure 2b) and [Cu]/[O] < 2.0 (Figure 2c). Nonuniform potential field of $Cu_2O_{1-\delta}$[1] shows that the potential mapping by KPFM is varied in nanoscale region, hence the work function for samples with oxygen vacancy. Kelvin images represent apex layer of the nanostructure surface with dark contrast (red), which corresponds to a lower work function with respect to the adjacent area. Surface potential is varied according to the tiny nanoprotrusion of the emitter surface, thus the electric field will be maximized at the lower work function surface rather than the higher. This nonuniform potential also generates a lateral electron tunneling through the material and will follow the lower potential path to emit form the surface, indicating field intensification at the apex region of the surface. Schematic field intensification has been analyzed in Supporting Information data. However, we should also think about the defects formation in the material, which will in general pin the work function. On the basis of our KPFM scanning measurement, we have found that the average surface potential values correspond to two different samples are –412 mV ([Cu]/[O] > 2.0) and –153 mV ([Cu]/[O] < 2.0), relative to the Pt-coated tips used in this study. We have kept all the factors that affect the KPFM data acquisition to minimize the errors in quantitative measurement. The distance between tip and sample surface, set to an optimized condition at 40 nm for all measurements reported here. The acquiring potential difference between the two type of samples corroborates our theoretical model.

2.3. Proposed Model with $Cu_2O_{1-\delta}$(111) Surface

As other cubic crystal, an ideal Cu_2O(111) surface having hexagonal symmetry, is non-polar with periodical arrangement of three consecutive stack of atomic layers. No single atomic layer parallel to the Cu_2O(111) surface contains both copper cations and oxygen anions. Each copper containing plane with four

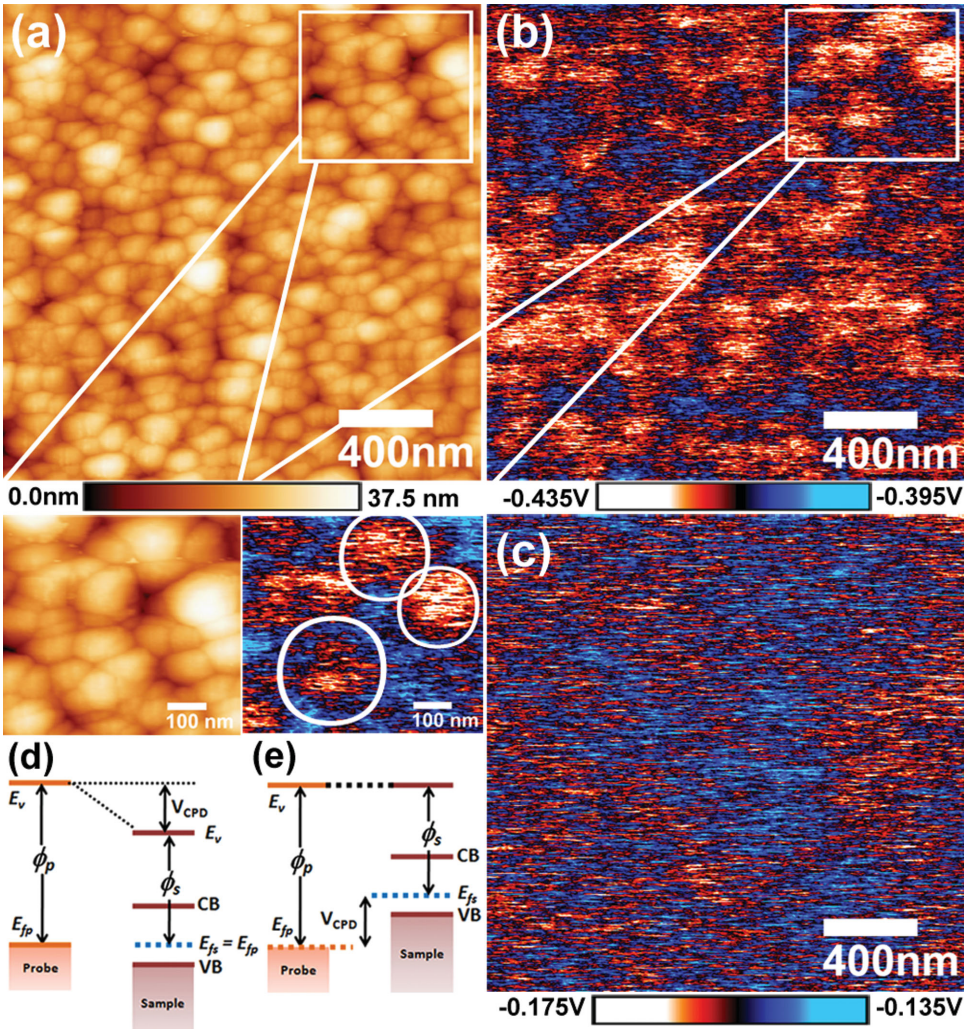

Figure 2. a) Shows the projection of AFM topographical images of $Cu_2O_{1-\delta}$ thin film with b) Localized potential mapping of the corresponding emitter surface. A close look of the scanning illustration indicates a clear variation of surface potential due to nanostructure. KPFM images represent apex layer of the nanostructure surface with orange contrast (indicated by white circle), which corresponds to a lower work function (ϕ) with respect to the adjacent area. This lower ϕ area corresponds to the apex of the emitter surface. c) Shows the potential mapping of standard sample with copper vacancy ($Cu_{2-\delta}O$). Schematic of electronic energy levels of the sample and AFM probe, when d) probe–sample are in electrical contact without biasing and e) with external bias (U_{DC}) which nullifies the CPD, i.e., probe-sample electrical force. Where E_{fs} and E_{fp} are the Fermi energy levels of the sample and AFM probe, respectively, and E_V is the vacuum energy level.

Cu^+ per surface unit cell is sandwiched between two oxygen containing plane with one O^{-2} per surface unit cell parallel to (111) surface. Thus, a three stack atomic layer repeat unit is necessary to satisfy stoichiometry and charge neutrality.[41,42] The unit cell of Cu_2O has been shown in Figure S3a, Supporting Information. A three stack atomic layer parallel to Cu_2O (111) surface of unit cell including four chemically different types of surface atoms, denoted by Cu_{CUS} (surface Cu that is coordinative unsaturated, i.e., singly coordinated Cu^+ cation), Cu_{CSA} (coordinative saturated Cu atom, i.e., doubly coordinated Cu^+ cation), O_{SUF} (outer most surface oxygen, i.e., fourfold coordinated O^{-2} anion), and O_{SUB} (subsurface oxygen, i.e., fourfold coordinated O^{-2} anion) was shown in Figure S3b, Supporting Information. As for the Cu_2O (111) surface, the oxygen atoms and its vacancies are most probably involved in the intrinsic defect mechanism and origin of impurity states and Fermi level pinning. Now when O^{-2} ion is removed from the O–Cu–O periodic tri-stack atomic layer, the materials with Cu_2O (111) surface will no more be stoichiometric, formed oxygen deficient $Cu_2O_{1-\delta}$ (111) surface. According to Mulliken´s concept of electronegativity,[43,44] each oxygen vacancy gives rise to four singly coordinate Cu^+ cation, reducing the ionic charge in order to maintaining the charge neutrality. These Cu atoms will be approaching themselves, trying to form Cu cluster with unshared Cu 3*d* state and partially reduces electro positivity of the cation. This makes effect on the electronic structure of $Cu_2O_{1-\delta}$ (111) surface. For bulk Cu_2O, valance band (VB) are composed of O 2*p* and Cu 3*d* orbital, indicating O 2*p*- Cu 3*d* hybridization.[45,46] Now as a result of O vacancy, the unshared Cu 3*d* state will be deploying toward the conduction band, attributing an impurity energy state in between the pure Cu_2O energy gap. This will act as a donor level of the

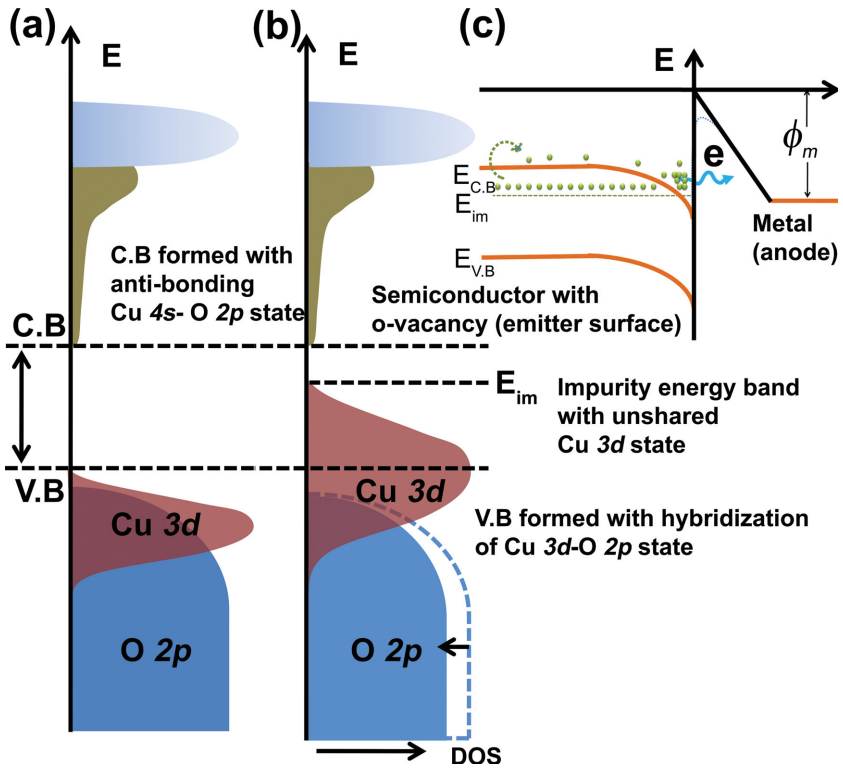

Figure 3. Schematic band structure of a) Cu_2O and b) $Cu_2O_{1-\delta}$ with impurity energy band formed by the unshared Cu 3*d* state. Arrows (from dotted blue line) indicate the decrease in the number of oxygen states and the accompanying rise in the Fermi level upon reduction. The band stretching of the Cu 3*d* state was supported by our theoretical model. c) Schematic of band bending with impurity donor state at the presence of electric field.

defect $Cu_2O_{1-\delta}$ (111) surface. A simple schematic diagram of the proposed electronic band structure with and without oxygen vacancy has been illustrated in **Figure 3**.

The model stipulates two things: 1) the total number of states in oxygen band decreases and 2) unshared Cu *3d* states stretching toward the conduction band. Therefore, the electrons that were situated in these state strews themselves over the valance band, generating a donor level. This will be causation of decrement of effective work function energy. The tunneling electrons will therefore easily be coming out from this donor level (or impurity level, E_{im}) enhancing the field emission phenomenon, a possible reason of oxygen vacancy. This argued aided thoroughly with our theoretical model and experimental results.

O_{vac} surfaces are formed according to the following reaction

$$Cu_2O(111) \rightarrow Cu_2O_{1-\delta}(111) + \delta\frac{1}{2}(O_2) + \delta\ddot{V}_o + \delta 2e' \quad (4)$$

Where $Cu_2O_{1-\delta}$ (111) denotes the Cu_2O (111) surface with oxygen vacancy at the rate of δ concentration per (2 × 2) super cell. $\ddot{V}_o$ means of oxygen vacancy and *e* is the electronic charge due to that vacancy.

The formation energy (E_{for}) for creating per O_{vac} can be described as

$$E_{for} = E\{Cu_2O_{1-\delta}(111)\} - E\{Cu_2O_1(111)\} + \mu(O) \quad (5)$$

where δ denotes the percentage of oxygen vacancies created on the Cu_2O_1 (111) plane and μ(O) is the chemical potential of oxygen, have two different values under oxygen deficiency and rich condition during experiments.[47] Our theoretical approach provides the formation energy to be about 0.32 eV and 2.08 eV for getting 2.08% (δ = 0.208) of oxygen vacancies in Cu_2O under oxygen deficiency and rich conditions, alluding the stable Cu_2O_1-δ (111) surfaces are easy to produce experimentally.

The entire explored Cu_2O nanostructures acquiring enhanced field emission with different oxygen vacancies were grown in highly single phase (111). Optimized deposition conditions have been eventuated (details are provided in Supporting Information) to achieve such. XRD of a typical sample ($Cu_2O_{1-\delta}$[1]) is shown in **Figure 4** inset. Samples were deposited in optimized atmosphere with limited surface diffusion and controlled motion of atoms.[1] The highest conformation of single phase $Cu_2O_{1-\delta}$ (111) with oxygen vacancy was indulged by XPS measurement. Figure 4a presents the survey spectra of typical $Cu_2O_{1-\delta}$ (111) sample. Pre-sputtering was performed for surface cleaning of the samples to avoid C 1*s* peak due to surface contamination by hydrocarbons. Highly pronounced Auger and photoelectron peaks of copper and oxygen were seen, while C 1*s* was practically on the noise level. The Cu 2*p* and O 1*s* photoelectron peaks and the Cu LMM and O KLL Auger peaks of Cu_2O are displayed in Figure 4a. A clear confirmation of pure single phase Cu_2O is observed in good agreement with those previously reported in ref. [48]. The core-level XPS spectrum of the Cu 2*p* line is shown in Figure 4b. Doublet peaks located at ≈932.2 eV and 952.1 eV were attributed to Cu $2p_{3/2}$ and Cu $2p_{1/2}$ in Cu_2O, respectively, which fits perfectly to Cu_2O phase.[49] However, the position attributed metallic copper is very close, i.e., at 932.65 eV.[49] Still, we also observe a small satellite peak S1 at about 946 eV, being a clear fingerprint of Cu_2O phase. A similar satellite peak S2 at about 943.6 eV has been also appeared. Since Cu $2p^{1/2}$ line is situated at 952.0 eV, the peak at 943.6 eV corresponds to its X-ray satellite peak, i.e., photoelectrons excited by MgKα3 line. In order to eliminate the chemical shift caused by the possible electrostatic charging of the material, modified Auger parameters were used as an additional confirmation that the dominant phase is Cu_2O and not metallic Cu. The measured modified Auger parameter estimated from the survey spectrum is 1849.2 eV ($\alpha' = E_K + E_B$) which confirms the presence of Cu_2O again. In the case of metallic Cu, α' should be about 1851.3 eV.[50] Figure 4c shows the core-level XPS spectrum of the O 1*s* line. Deconvolution of O 1*s* peak using Shirley background, gives a dominant peak position at 530.4 eV, which fits very well to the position for Cu_2O phase reported elsewhere,[49] indicating the oxygen atoms that are bonded with copper. The second contribution is at 531.7 eV

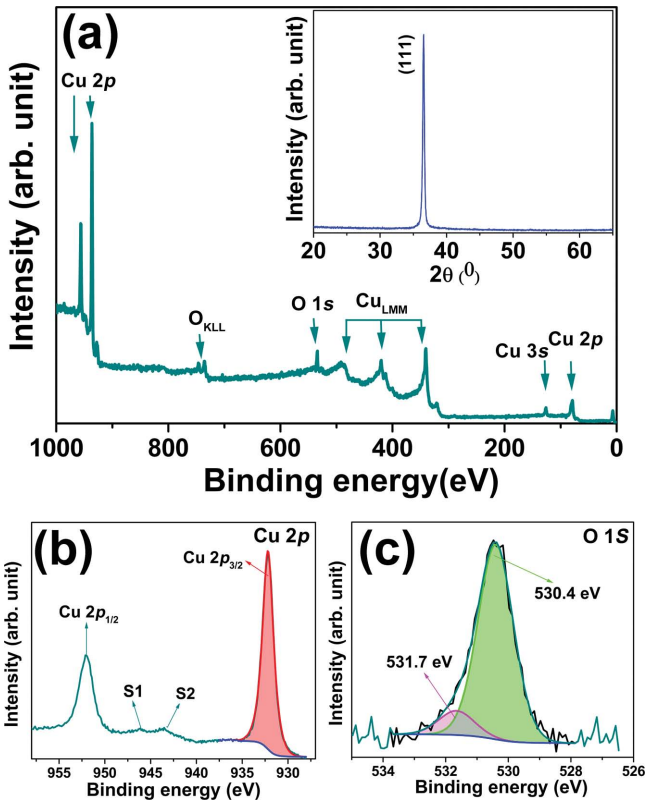

Figure 4. a) XPS survey of the typical $Cu_2O_{1-\delta}$[1] nanostructure. Inset: Shows XRD spectrum of the corresponding sample indicating the highly oriented (111) surface plane. b,c) Core-level XPS of Cu 2*p* and O 1*s* spectra.

which is very small in intensity can be part of some C–O bonds from the surface impurity. The results of the composition analysis, based on the intensities of the O 1*s* and Cu $2p_{3/2}$ lines are given in **Table 2**. Clearly, the amount of oxygen is roughly two times smaller than that of copper which already suggests that Cu_2O phase is dominant. However, the ration of [Cu]/ [O] is greater than two, indicating enriched copper in the film. Based on this study it can be confirmed that the films were Cu rich with the formation of oxygen vacancy and can be attributed to $Cu_2O_{1-\delta}$. The phenomenon was in good agreement with our theoretical model. It seems that deposition at oblique incidence contributes to small reduction in oxygen to copper composition ratio, as the films were deposited in highly controlled atmosphere which producing strain during atomic growth. Strain changes the relative position of the atoms compose the crystal,

Table 2. Surface composition of copper and oxygen measured by XPS.

Sample	Oxygen		Copper [%]	[Cu]/[O] in $Cu_2O_{1-\delta}$
	Cu-oxide [%]	Impurities [%]		
$Cu_2O_{1-\delta}$[1]	28.5	3.5	68	≈2.38
$Cu_2O_{1-\delta}$[2]	29.4	3.6	67	≈2.27
$Cu_2O_{1-\delta}$[3]	30.9	4.1	65	≈2.10

and thus effects the spatial interaction between atoms, generating a vacancy.

We model the structure of the Cu_2O (111) surface with and without oxygen vacancy (O_{vac}) and estimate the density of states (DOS), work-function and Mullikan charge. **Figure 5**a,b shows the side and top view of pure (2 × 2)Cu_2O (111) supercell with oxygen atom in the top layer. According to our hypothesis, we study the Cu_2O (111) surface with O vacancy, which has been removed from the arbitrary lattice site. Figure 5c represents the relaxed structure of O vacant Cu_2O (111) surface. The four big pink balls (shown in Figure 5c) indicate the Cu atoms (only bound to single oxygen atom) around O vacancy and the comparatively small pink balls are the bounded Cu atoms (with two oxygen atom). By deoxygenating this surface, the O vacancy enhanced the Cu^+–Cu^+ interactions; stretching of distance between Cu atom with other O atoms, i.e., increasing of bond length. Consequently, the unsaturated Cu atoms will try to make little closer bond (interaction increases) among themselves to form metal clusters, subsequently the increase of electron density around vacancy is observed. The Mulliken charge analysis shows that the four Cu atoms (neighbor of O_{vac} atom) are less positive revealed increase of unshared *d* electron around vacancy. Figure 5d demonstrates the total density of states (TDOS) of pure and O vacant Cu_2O (111) using PBE and PBE+U functional. The direct band gap (E_g) of copper oxide is about 2.2 eV, whereas the simple DFT results indicate the gap is around 0.4–0.5 eV, which underestimate the E_g more than 50% than expected for a typical DFT error, shown in Figure 5d. Hence we consider the U parameter for better understanding of electronic structure to explain field emission property. The partial DOS (PDOS) of the surface with oxygen vacancy shows that the occupied state form unshared Cu 3*d* electrons (indicated by 1 in Figure 5c) just at the top of the valance band are stretched. The investigation of PDOS for different Cu 3*d* state for shared (2) and unshared (1) electrons with O 2*p* state are shown in Figure 5e, indicating shifting of *d*-band center toward vacuum level. The unshared *d* electrons form a donor state claimed as an impurity energy state (E_{im}), cause shifting of Fermi level toward vacuum, shown in our schematic band structure (Figure 3). This will take part in work function level pinning. **Figure 6** demonstrates the electrostatic potential as a function of fractional coordinate for bulk and $Cu_2O_{1-\delta}$. The estimated work function is about 4.97 eV for O vacant Cu_2O (111) surface (2.08%), which is 0.28 eV lesser than pure Cu_2O (111) surface. Further calculation on the electrostatic potentials as a function of fractional coordinates for two different Oxygen vacancy percentages (4.16% and 6.25%) yields the work function energy 4.84 and 4.76 eV, respectively. The electrostatic potential profiles have been shown in Figure S6, Supporting Information. To calculate the work function, we consider the (2 × 2) supercell of Cu_2O (111) and replace one, two, and three O atoms per supercell, respectively. Results indicate that the increase of oxygen vacancy will decrease the work function, leading the Fermi-level pinning. This is also supported by our KPFM image analysis. This attributes that the barrier height to tunnel electron in case of O_{vac} is lower, which will additionally increase the field emission current (apart from geometrical enhancement factor). The electronic structures suggest that the oxygen vacancies decrease the work

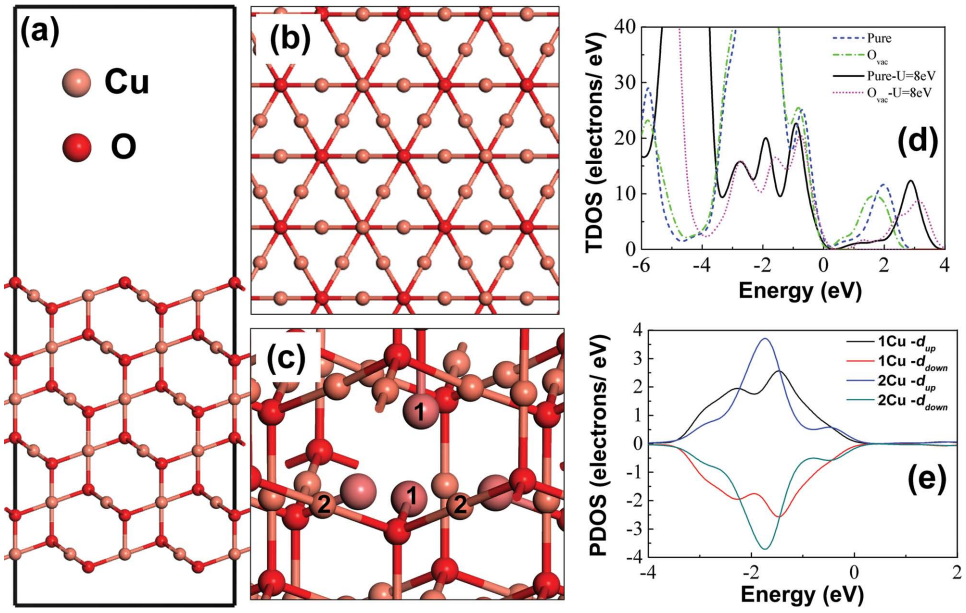

Figure 5. a,b) Side and top view of Cu_2O (111) thin film consider as the system for further calculation. c) O vacant Cu_2O (111), four big balls represent here the neighbor Cu atoms of vacant O atom. d) Total density of states (TDOS) of pure and O_{vac} Cu_2O using PBE and PBE+U methods. e) Projected DOS (PDOS) of the Cu 3*d* state for share (indicated by Cu-2) and unshared (indicated by Cu-1) with oxygen atom. The stretching of the Cu 3*d* states has been observed for uncoordinated Cu atom.

function and so enhance the electron tunnelling proficiency of the surfaces to some extent.

3. Conclusion

The presented results on electron tunneling behavior of Cu_2O nanostructure are quite interesting and dramatic. The Cu_2O nanostructure was deposited in completely optimized condition to get better field emission performance. A potential field emission from the emitter surface has been observed at very low turn-on and threshold field which makes it comparatively more efficient in emission device application. The emitter has been shown stability at 1 mA cm^{-2} current density for 2 h. The materials were entirely analyzed as per electron tunneling mechanism with defect structure. A theoretical model has been employed with oxygen vacancy to attribute the tunneling mechanism. XPS and KPFM measurements have been performed to consolidate the proposed theoretical model. This paper is a part of theoretical "tidy up" to evaluate the level of electron tunneling mechanism from Cu_2O nanostructure surface and a step toward further applications.

4. Experimental Section

The fabrication of nanostructure Cu_2O on silicon and ITO coated glass substrates was performed by GLAD technique. A detail of deposition technique has been given in a previous article published by this group.[1] A unique nanostructure of highly dense Cu_2O arrays with tiny cracked surface has been synthesized. Difference in nanostructure formation was observed with a changing sputtering pressure. Details of the sputtering have been discussed in Supporting Information. As deposited samples were characterized using X-ray diffraction (XRD, PANalytical X'Pert Pro Diffractometer), scanning electron microscopy (SEM-FIB, Zeiss Auriga Crossbeam microscope), and atomic force microscopy (AFM, Asylum MFP-3D). For the purpose of investigating the nanostructure geometry of Cu_2O, samples deposited on silicon were cut to fix it in vertical by clamp for observing the cross-sectional view by SEM. Nano-sized miniature arrays of apex on the sample surface was analyzed by 3D image of AFM.

X-Ray Photoelectron Spectroscopy: XPS measurement has been performed on a VSW XPS system with the Class 100 energy analyzer being a part of an experimental setup assembled for surface investigation[51] using the nonmonochromatic MgK_α line (photon energy of 1256.3 eV). For the energy axis calibration, Ag (110) and polycrystalline Au samples (previously cleaned by ion sputtering) were used. The energy was calibrated to the peak position of Ag $3d_{5/2}$ (binding energy of 368.22 eV) and Au $4f_{7/2}$(binding energy of 83.96 eV) lines. The detailed XPS lines were taken in FAT 22 mode with 0.1 eV of energy step, while the survey spectra were taken in FAT 44 mode with 0.5 eV energy step. The valence band was taken in the FAT 10 mode in order to provide the highest possible resolution. The composition analysis has been performed using the sensitivity factors from,[52] which appear to work very well for this system. The samples were sputter cleaned using 3 keV Ar^+ ions prior to the analysis.

Field Emission: Field emission was carried out by a simple diode configuration in a vacuum chamber under a pressure of 1.3×10^{-5} Pa at room temperature. The schematic illustration is shown in Figure 1b. A flat panel anode metallic probe is equipped in a vacuum chamber. A micro-gauge variable stepper has been employed with anode plate to precisely keep the separation between emitter surfaces to anode plate. The silicon substrate with nanostructure thin film was performed for our field emission device.

Computational Details: We used the CAmbridge Serial Total Energy Package (CASTEP).[53] Ultrasoft pseudopotentials were used,[54] and the plane-wave basis set was used with the energy cutoff of 400 eV. The gradient corrected Perdew—Burke–Ernzerhof (PBE) functional was employed to describe the electrons exchange-correlation potential.[55] The PBE+U approach[56] as in CASTEP code has been taken into account

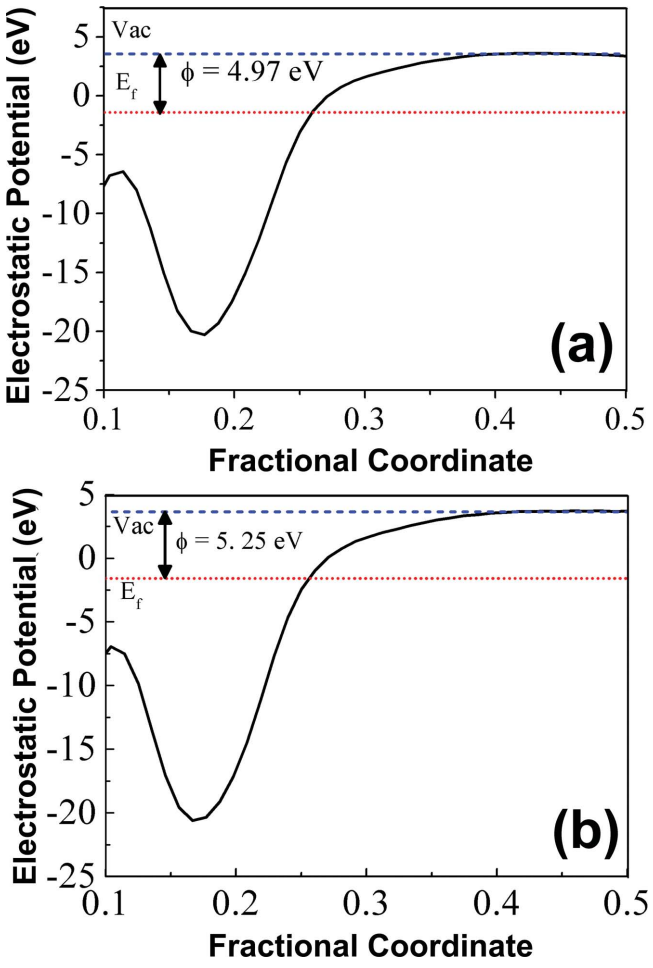

Figure 6. Demonstrate the electrostatic potential as function of fractional coordinates of a) pure Cu_2O and b) 2.08% O vacant Cu_2O(111) thin film. Vacuum potential is indicate by Vac, work function is denoted as ϕ and Fermi level is denoted as E_f.

for the on-site Coulomb repulsion of Zn 3*d* electrons. The geometry optimization in CASTEP code was performed with using Broyden–Fletcher–Goldfarb–Shanno (BFGS) scheme until the total energy converged within 10^{-5} eV atom^{-1} with the maximum force being less than 0.03 eV Å^{-1} and with the maximum displacement less than 0.001 Å.[57]

Supporting Information

Supporting Information is available from the Wiley Online Library or from the author.

Acknowledgements

This work was partially supported by the Portuguese Science and Technology Foundation (FCT), Ministry for Education and Science (MEC), under PEST-C/CTM/LA0025 (Strategic Project – LA 25 – 2013–2014), EXCL/CTM-NAN/0201/2012 and by the European Commission under project INVISIBLE (FP7 ERC Grant No. 228144). S.N. is supported by FCT-MEC under fellowships SFRH/BPD/70367/2010. Also in the section of theoretical study, we are also grateful to Professor Carter group for their valuable discussion. R.T. thanks science and engineering research board (SERB), India for the financial support (Grant No. SB/FTP/PS028/2013).

Received: August 24, 2014
Revised: October 31, 2014
Published online: December 23, 2014

[1] S. Nandy, G. Goncalves, J. V. Pinto, T. Busani, V. Figueiredo, L. Pereira, R. F. Paiva Martins, E. Fortunato, *Nanoscale* **2013**, *5*, 11699.
[2] L.-J. Pegg, R. A. Hatton, *ACS Nano* **2012**, *6*, 4722.
[3] J. A. Anta, *Curr. Opin. Colloid Interface Sci.* **2012**, *17*, 124.
[4] H. Shi, K. Yu, F. Sun, Z. Zhu, *Cryst. Eng. Commun.* **2012**, *14*, 278.
[5] K. Yu, Y. S. Zhang, F. Xu, Q. Li, Z. Q. Zhu, Q. Wan, *Appl. Phys. Lett.* **2006**, *88*, 153123.
[6] J. Liang, G. Zhang, *ACS Appl. Mater. Interfaces* **2012**, *4*, 6053.
[7] Y. Guo, W. Guo, *J. Phys. Chem. C* **2012**, *117*, 692.
[8] D. Ye, S. Moussa, J. D. Ferguson, A. A. Baski, M. S. El-Shall, *Nano Lett.* **2012**, *12*, 1265.
[9] S. Goswami, U. N. Maiti, S. Maiti, S. Nandy, M. K. Mitra, K. K. Chattopadhyay, *Carbon* **2011**, *49*, 2245.
[10] S. W. Joo, A. N. Banerjee, *J. Appl. Phys.* **2010**, *107*, 114317.
[11] W. Zhu, G. P. Kochanski, S. Jin, *Science* **1998**, *282*, 1471.
[12] W. J. Kim, J. S. Lee, S. M. Lee, K. Y. Song, C. N. Chu, Y. H. Kim, *ACS Nano* **2010**, *5*, 429.
[13] R. H. Flower, L. Nordheim, *Proc. Royal Soc. London. Ser. A* **1928**, *119*, 173.
[14] P. A. Chatterton, *Proc. Phys. Soc.* **1966**, *88*, 231.
[15] L. Y. Isseroff, E. A. Carter, *Chem. Mater.* **2013**, *25*, 253.
[16] M. Nolan, S. D. Elliott, *Phys. Chem. Chem. Phys.* **2006**, *8*, 5350.
[17] D. O. Scanlon, B. J. Morgan, G. W. Watson, *Phys. Rev. Lett.* **2009**, *103*, 096405.
[18] D. Lim, R. Haight, M. Copel, E. Cartier, *Appl. Phys. Lett.* **2005**, *87*, 072902.
[19] A. Klein, *Thin Solid Films* **2012**, *520*, 3721.
[20] Y. Akasakai, G. Nakamura, K. Shiraishi, N. Umezawa, K. Yamabe, O. Ogawa, M. Lee, T. Amiaka, T. Kasuya, H. Watanabe, T. Chikyow, F. Ootsuka, Y. Nara, K. Nakamura, *Jpn. J. Appl. Phys.* **2006**, *45*, L1289.
[21] H. Yamaguchi, K. Murakami, G. Eda, T. Fujita, P. Guan, W. Wang, C. Gong, J. Boisse, S. Miller, M. Acik, K. Cho, Y. J. Chabal, M. Chen, F. Wakaya, M. Takai, M. Chhowalla, *ACS Nano* **2011**, *5*, 4945.
[22] Y.-M. Chang, M.-C. Liu, P.-H. Kao, C.-M. Lin, H.-Y. Lee, J.-Y. Juang, *ACS Appl. Mater. Interfaces* **2012**, *4*, 1411.
[23] X. Zhou, T. Lin, Y. Liu, C. Wu, X. Zeng, D. Jiang, Y.-a. Zhang, T. Guo, *ACS Appl. Mater. Interfaces* **2013**, *5*, 10067.
[24] H.-H. Lin, C.-Y. Wang, H. C. Shih, J.-M. Chen, C.-T. Hsieh, *J. Appl. Phys.* **2004**, *95*, 5889.
[25] R. G. Forbes, C. J. Edgcombe, U. Valdrè, *Ultramicroscopy* **2003**, *95*, 57.
[26] J. Wang, L. Wei, L. Zhang, J. Zhang, H. Wei, C. Jiang, Y. Zhang, *CrystEngComm* **2013**, *15*, 1296.
[27] L. I. Bendavid, E. A. Carter, *J. Phys. Chem. B* **2013**, *117*, 15750.
[28] H. Wu, N. Zhang, H. Wang, S. Hong, *J. Theor. Comput. Chem.* **2012**, *11*, 1261.
[29] U. A. Palnitkar, R. V. Kashid, M. A. More, D. S. Joag, L. S. Panchakarla, C. N. R. Rao, *Appl. Phys. Lett.* **2010**, *97*, 063102.
[30] Y. Wang, S. Li, H. Shi, K. Yu, *Nanoscale* **2012**, *4*, 7817.
[31] Q. Tang, T. Li, X. Chen, D. Yu, Y. Qian, *Solid State Commun.* **2005**, *134*, 229.
[32] M. Deo, D. Shinde, A. Yengantiwar, J. Jog, B. Hannoyer, X. Sauvage, M. More, S. Ogale, *J. Mater. Chem. C* **2012**, *22*, 17055.

[33] W. Zhao, R.-Z. Wang, Z.-W. Song, H. Wang, H. Yan, P. K. Chu, *J. Phys. Chem. C* **2012**, *117*, 1518.
[34] J. G. Simmons, *J. Appl. Phys.* **1963**, *34*, 1793.
[35] J. M. Beebe, B. Kim, J. W. Gadzuk, C. Daniel Frisbie, J. G. Kushmerick, *Phys. Rev. Lett.* **2006**, *97*, 026801.
[36] J. W. Gadzuk, E. W. Plummer, *Rev. Mod. Phys.* **1973**, *45*, 487.
[37] A. F. Yatsenko, *Phys. Status Solidi (a)*, **1970**, *1*, 333.
[38] L. M. Baskin, O. I. Lvov, G. N. Fursey, *Phys. Status Solidi (b)*, **1971**, *47*, 49.
[39] W. Melitz, J. Shen, A. C. Kummel, S. Lee, *Surf. Sci. Rep.* **2011**, *66*, 1.
[40] M. Bieletzki, T. Hynninen, T. M. Soini, M. Pivetta, C. R. Henry, A. S. Foster, F. Esch, C. Barth, U. Heiz, *Phys. Chem. Chem. Phys.* **2010**, *12*, 3203.
[41] K. H. Schulz, D. F. Cox, *Phys. Rev. B* **1991**, *43*, 1610.
[42] P. W. Tasker, *J. Phys. C: Solid State Phys.* **1979**, *12*, 4977.
[43] R. S. Mulliken, *J. Chem. Phys.* **1934**, *2*, 782.
[44] R. S. Mulliken, *J. Chem. Phys.* **1935**, *3*, 573.
[45] S. Nandy, A. Banerjee, E. Fortunato, R. Martins, *Rev. Adv. Sci. Eng.* **2013**, *2*, 273.
[46] M. M. Islam, B. Diawara, V. Maurice, P. Marcus, *J. Mol. Struct. THEOCHEM* **2009**, *903*, 41.
[47] R. Thapa, B. Saha, K. K. Chattopadhyay, *Comput. Mater. Sci.* **2010**, *49*, 363.
[48] P. Wang, Y. H. Ng, R. Amal, *Nanoscale* **2013**, *5*, 2952.
[49] M. C. Biesinger, L. W. M. Lau, A. R. Gerson, R. S. C. Smart, *Appl. Surf. Sci.* **2010**, *257*, 887.
[50] http://www.xpsfitting.com/search/label/Copper, (accessed: December, 2014).
[51] O. Teodoro, J. Silva, A. M. C. Moutinho, *Vacuum* **1995**, *46*, 1205.
[52] D. Briggs, *Practical Surface Analysis*, 2nd ed., J. Willey & Sons, New York, **1993**.
[53] M. D. Segall, J. D. L. Philip, M. J. Probert, C. J. Pickard, P. J. Hasnip, S. J. Clark, M. C. Payne, *J. Phys. Condens. Matter.* **2002**, *14*, 2717.
[54] D. Vanderbilt, *Phys. Rev. B* **1990**, *41*, 7892.
[55] J. P. Perdew, K. Burke, M. Ernzerhof, *Phys. Rev. Lett.* **1996**, *77*, 3865.
[56] M. Cococcioni, S. de Gironcoli, *Phys. Rev. B* **2005**, *71*, 035105.
[57] B. G. Pfrommer, M. Côté, S. G. Louie, M. L. Cohen, *J. Comput. Phys.* **1997**, *131*, 233.